AN ANALYSIS OF NORMAL FORCE COEFFICIENT RESULTS FOR THE VLS CENTRAL BODY

Enda Dimitri Vieira Bigarelli – biga@h8.ita.br
Centro Técnico Aeroespacial, Instituto Tecnológico de Aeronáutica
CTA/ITA/IEAA – 12228-900 – São José dos Campos, SP, Brasil
Lucas Rubiano de Souza Cruz – rubiano@h8.ita.br
Centro Técnico Aeroespacial, Instituto Tecnológico de Aeronáutica
CTA/ITA/IEAA – 12228-900 – São José dos Campos, SP, Brasil
João Luiz F. Azevedo – azevedo@iae.cta.br
Centro Técnico Aeroespacial, Instituto de Aeronáutica e Espaço
CTA/IAE/ASE-N – 12228-904 – São José dos Campos, SP, Brasil

Abstract. *This work presents a study of VLS aerodynamics which uses the capability implemented at IAE to simulate 3-D flows over typical launch vehicle configurations at angle of attack. This capability is further used to determine normal loads over the VLS main body configuration at an angle-of-attack flight. The numerical simulations performed use the compressible Euler formulation, discretized in a finite difference context for general curvilinear coordinates. A 5-stage, explicit Runge-Kutta time-march procedure is used and the spatial discretization employs central differences. Numerical results are compared with available experimental data for the VLS and they are used to assess the aerodynamic characteristics of the VLS central body at angle of attack.*

Keywords: *Launch vehicle, CFD, Three-dimensional flow, Flow at angle of attack, Supersonic flow.*

1. INTRODUCTION

Satellite launchers, such as the first Brazilian satellite launcher (VLS), currently considered at Instituto de Aeronáutica e Espaço (IAE), are vehicles typically designed to fly at very low angles of attack. Nevertheless, the lateral loads that arise over such vehicles, even at small angles of attack, are significant and their accurate calculation is of fundamental importance in the vehicle design process. Thus, the loads required for the structural design of the vehicle as well as the flight dynamics stability characteristics necessary for control system design can be determined. In this sense, IAE has looked for methods to obtain this data using CFD techniques. Zdravistch and Azevedo (1990) have performed axisymmetric calculations with very good results concerning the physical representation over the VLS. Azevedo, Zdravistch and Silva (1991) and Azevedo *et al.* (1996) have also performed three-dimensional inviscid computations over the VLS with good agreement with experimental data. More recently, calculations over sounding

rocket configurations, namely the Sonda IIIA, were reported by Bigarelli, Mello and Azevedo (1999).

In the present work, efforts are made in order to analyze normal force coefficient results for the VLS central body, using a formulation similar to the one described by Bigarelli and Azevedo (1999). The solver used is a 3-D finite difference code written for general, body-conforming, curvilinear coordinate systems and solves the compressible Euler equations. The governing equations are discretized by a central finite difference scheme. Time stepping uses an explicit 2nd-order, 5-stage Runge-Kutta scheme.

Computations are performed for the VLS main body configuration at freestream Mach numbers of 1.25, 2.00 and 3.00 and angles of attack of 0, 2 and 4 deg. Pressure coefficient distributions along the vehicle wall are obtained. An azimuthal integration of these pressure coefficients is, then, performed in order to calculate the normal force distributions, $dC_N/d(x/L)$, and the normal coefficient slope distribution with angle of attack, $dC_{N_\alpha}/d(x/L)$, along the vehicle main body. Then, the correctness of these results is assessed through a comparison with available wind tunnel data, as presented by Augusto Neto (1991).

2. THEORETICAL FORMULATION

The numerical code used in this work solves the 3-D, compressible Euler equations. These equations can be written in strong conservation-law form for general, body-conforming, curvilinear coordinates (Pulliam and Steger, 1980, and Azevedo, Zdravistch and Silva, 1991) as

$$\frac{\partial \overline{Q}}{\partial \tau} + \frac{\partial \overline{E}}{\partial \xi} + \frac{\partial \overline{F}}{\partial \eta} + \frac{\partial \overline{G}}{\partial \zeta} = 0 \ . \tag{1}$$

The vector of conserved quantities, $\overline{Q}$, can be defined as

$$\overline{Q} = J^{-1} \left[\begin{array}{ccccc} \rho & \rho u & \rho v & \rho w & e \end{array} \right]^{\mathrm{T}} \ , \tag{2}$$

and the inviscid flux vectors, $\overline{E}$, $\overline{F}$ and $\overline{G}$, can be written as

$$\overline{E} = J^{-1} \left\{ \begin{array}{c} \rho U \\ \rho u U + p\xi_x \\ \rho v U + p\xi_y \\ \rho w U + p\xi_z \\ (e+p)U - p\xi_t \end{array} \right\} \ , \qquad \overline{F} = J^{-1} \left\{ \begin{array}{c} \rho V \\ \rho u V + p\eta_x \\ \rho v V + p\eta_y \\ \rho w V + p\eta_z \\ (e+p)V - p\eta_t \end{array} \right\} \ ,$$

$$\overline{G} = J^{-1} \left\{ \begin{array}{c} \rho W \\ \rho u W + p\zeta_x \\ \rho v W + p\zeta_y \\ \rho w W + p\zeta_z \\ (e+p)W - p\zeta_t \end{array} \right\} \ . \tag{3}$$

In the usual CFD nomenclature, being adopted in the present work, ρ is the density, u, v and w are the Cartesian velocity components, p is the pressure, and e is the total energy per unit volume. The pressure is obtained from the equation of state for perfect gases, written as

$$p = (\gamma - 1) \left[e - \frac{1}{2} \rho \left(u^2 + v^2 + w^2 \right) \right] \ , \tag{4}$$

where γ is the ratio of specific heats. The contravariant velocity components, U, V and W, can be written as

$$\begin{aligned} U &= \xi_t + \xi_x u + \xi_y v + \xi_z w \ , \\ V &= \eta_t + \eta_x u + \eta_y v + \eta_z w \ , \\ W &= \zeta_t + \zeta_x u + \zeta_y v + \zeta_z w \ . \end{aligned} \tag{5}$$

Throughout this work, the curvilinear coordinate system is defined such that ξ is the rocket longitudinal direction, positive downstream, η is the wall-normal direction, and ζ is the circumferential direction. This coordinate system is obtained from the transformation of variables

$$\tau = t \ , \qquad \xi = \xi(x,y,z,t) \ , \qquad \eta = \eta(x,y,z,t) \ , \qquad \zeta = \zeta(x,y,z,t,) . \tag{6}$$

Expressions for the Jacobian of the transformation, J, and for the various metric terms can be found in Pulliam and Steger (1980), among other references.

3. NUMERICAL IMPLEMENTATION

The governing equations can be discretized in a finite difference context. The spatial discretization adopted uses a central difference type algorithm plus explicitly added artificial dissipation terms in order to control nonlinear instabilities. The equations, fully discretized in space, can be written as

$$\left(\frac{\partial \overline{Q}}{\partial \tau} \right)_{i,j,k} = -\mathrm{RHS}_{i,j,k} \ . \tag{7}$$

The right-hand side operator of Eq. (7) is defined as

$$\begin{aligned} \mathrm{RHS}_{i,j,k} &= \frac{1}{2\,\Delta\xi} \left(\overline{E}_{i+1,j,k} - \overline{E}_{i-1,j,k} \right) + \frac{1}{2\,\Delta\eta} \left(\overline{F}_{i,j+1,k} - \overline{F}_{i,j-1,k} \right) \\ &+ \frac{1}{2\,\Delta\zeta} \left(\overline{G}_{i,j,k+1} - \overline{G}_{i,j,k-1} \right) \ , \end{aligned} \tag{8}$$

where $\Delta\xi = \Delta\eta = \Delta\zeta = 1$ for the general curvilinear coordinate case. An anisotropic, scalar artificial dissipation model, as described in Turkel and Vatsa (1994), is used. This scheme is nonlinear and allows a switch between second and fourth difference artificial dissipation terms, which is very important in capturing shock waves throughout the flow without degrading the overall order of accuracy of the method.

Time march uses an explicit, 2nd-order, 5-stage Runge-Kutta scheme, as described in Jameson, Schmidt and Turkel (1981) and Jameson and Mavriplis (1986), which can be written as

$$\begin{aligned} \overline{Q}^{(0)}_{i,j,k} &= \overline{Q}^{n}_{i,j,k} \ , \\ \overline{Q}^{(\ell)}_{i,j,k} &= \overline{Q}^{(0)}_{i,j,k} - \alpha_\ell \, \Delta t_{i,j,k} \, \mathrm{RHS}^{(\ell-1)}_{i,j,k} \ , \qquad \ell = 1,2,\ldots,5, \\ \overline{Q}^{n+1}_{i,j,k} &= \overline{Q}^{(5)}_{i,j,k} \ . \end{aligned} \tag{9}$$

In the previous expressions, Δt stands for the time step, and n and $n+1$ indicate the property values at the start and at the end of each time step. Further details of the time-marching scheme implemented, including variable time-step option, can be found in Bigarelli, Mello and Azevedo (1999).

4. BOUNDARY CONDITIONS

For the configurations of interest here, the types of boundary conditions that should be considered include solid walls, far field boundaries, symmetry, upstream centerline and downstream (exit) conditions. For the rocket wall, the velocity vector is made tangent to the wall. Zero-order extrapolation of the other conserved variables from the computational plane adjacent to the wall is used in order to obtain the remaining boundary data. The upstream centerline is a singularity of the coordinate transformation and, hence, an adequate treatment of this boundary must be provided. In the present case, the approach consists in extrapolating the property values from the adjacent longitudinal plane and in averaging the extrapolated values in the azimuthal direction in order to define the updated properties at the upstream centerline. At the exit plane,

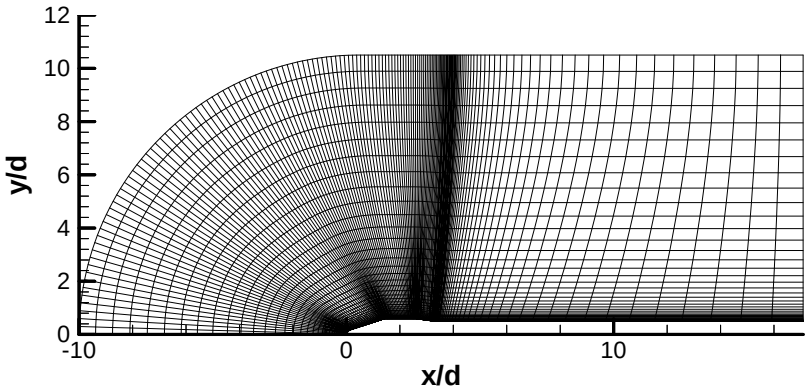

Figure 1: Overall view of a plane from the VLS 3-D grid used for numerical simulations.

the boundary conditions are implemented through the use of the 1-D characteristic relations for the 3-D Euler equations. The interested reader is referred to the work of Azevedo, Fico and Ortega (1995) for further details on the use of 1-D characteristic relations for boundary condition implementation. Freestream properties are assumed at the far field boundaries.

Furthermore, in order to reduce computational costs, the grid used in the numerical simulations performed was generated for half a body in the azimuthal direction. This simplification is valid for the cases assessed in this work because low angles of attack are considered. This condition implies a symmetric flow about the pitching plane, as indicated in Ying (1986) among other references. Hence, symmetry is applied in the pitching plane using two auxiliary planes, namely, $k = 1$ and $k = kmax$. Those extra planes are added, respectively, before the leeside and after the windside pitching plane. The symmetry conditions can be written as

$$
\begin{array}{ll}
\rho_{i,j,1} = \rho_{i,j,3} \ , & \rho_{i,j,kmax} = \rho_{i,j,kmax-2} \ , \\
(\rho u)_{i,j,1} = (\rho u)_{i,j,3} \ , & (\rho u)_{i,j,kmax} = (\rho u)_{i,j,kmax-2} \ , \\
(\rho v)_{i,j,1} = -(\rho v)_{i,j,3} \ , & (\rho v)_{i,j,kmax} = -(\rho v)_{i,j,kmax-2} \ , \\
(\rho w)_{i,j,1} = (\rho w)_{i,j,3} \ , & (\rho w)_{i,j,kmax} = (\rho w)_{i,j,kmax-2} \ , \\
e_{i,j,1} = e_{i,j,3} \ , & e_{i,j,kmax} = e_{i,j,kma-1} \ ,
\end{array}
\tag{10}
$$

where $k = 2$ and $k = kmax - 1$ are the azimuthal computational planes defined along the physical pitching plane. The resulting grid, including the additional planes, has $155 \times 65 \times 21$ points in the longitudinal, wall-normal and azimuthal directions, respectively. A longitudinal plane of the grid can be seen in Fig. 1.

5. RESULTS AND DISCUSSION

The following figures show a comparison between numerical and experimental results. In a general form, good agreement between those results are obtained. The numerical curves are qualitatively similar to the experimental ones. One can also verify that shock wave and expansion regions are well captured by the numerical procedure. Nevertheless, in some regions of the flow, computational simulations may not seem to be accurate when compared to wind tunnel results. This behavior is well explained by the fact that, in those regions, viscosity and interactions between shock waves and boundary layer play a fundamental role in the flow configuration. Since the numerical code used solves the Euler equations, those viscous flow phenomena cannot be represented in the results. Furthermore, in the great majority of cases studied, numerical coefficient distributions have smaller magnitude than the experimental ones. A general explanation for this fact is that the boundary layer alters the flow around the body. In the leeside region, boundary layer growth is more pronounced due to the positive angle of attack. Thus, the local flow sees an apparent body which is bluffer than the original one. This causes additional flow acceleration, which, in turn, yields lower pressure coefficient distributions along the rocket wall when compared to the inviscid case. Hence, in the azimuthal integration

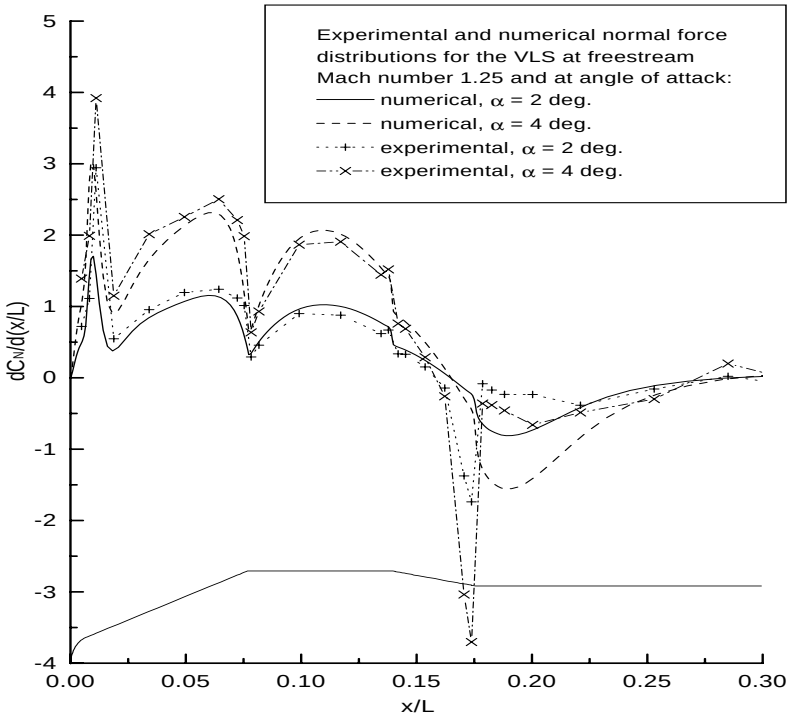

Figure 2: Numerical results for normal force coefficient distribution compared to experimental data for VLS at $\alpha = 2$ and 4 deg. and $M_\infty = 1.25$.

of these pressure coefficients, normal forces calculated with an inviscid analysis are smaller than the ones obtained from the actual experimental data.

Figure 2 presents computational simulation and wind tunnel results for the VLS main body at freestream Mach number $M_\infty = 1.25$ and at angles of attack $\alpha = 2$ and 4 deg. Numerical and experimental curves are qualitatively alike, except for the boattail region. Furthermore, the shock wave in this region is well captured by the numerical procedure. Nevertheless, a drop in the normal force coefficient is obtained. A jump in the normal force distribution, as encountered in the experimental data, was expected. As one could expect, aerodynamics in this region is very dependent on viscous flow phenomena, such as boundary layer separation due to adverse pressure gradient and shock-boundary layer interaction. Hence, it is understandable that the inviscid numerical code used in this work is not able to capture the exact flow behavior. One can also verify that the solver captures very well the position of the expansion waves on the afterbody corners. This is characterized by a drop of the local normal force coefficient. In those regions, the boundary layer decreases with the acceleration applied to the flow through the expansion and, thus, viscosity effects are not predominant. Hence, numerical and experimental results are very similar to each other.

One can also observe in Fig. 2 that the numerical normal force coefficient distributions, in the forebody cone of the rocket, are lower than the experimental distributions. As already seen, this is explained by the growth of the boundary layer, in the leeside region, because of the angle of attack. This causes an acceleration of the flow, which decreases the pressure coefficient in the region, if compared with an inviscid simulation. Thus, in the azimuthal integration of the pressure, the experimental results are greater than the inviscid ones. In the payload fairing region, nevertheless, the experimental distributions are now lower than the numerical ones. This can be partially explained by the fact that, in this region, the boundary layer tends to decrease in its size, because of the expansion at the end of the first cone. This balances the effect of the angle of attack in the growth of the boundary layer. Thus, in result, the experimental normal force coefficient distribution are closer to the inviscid one. Finally, both results converge to zero after the boattail. This was expected, since the flow tends to return to the freestream condition, for both the leeside and windside.

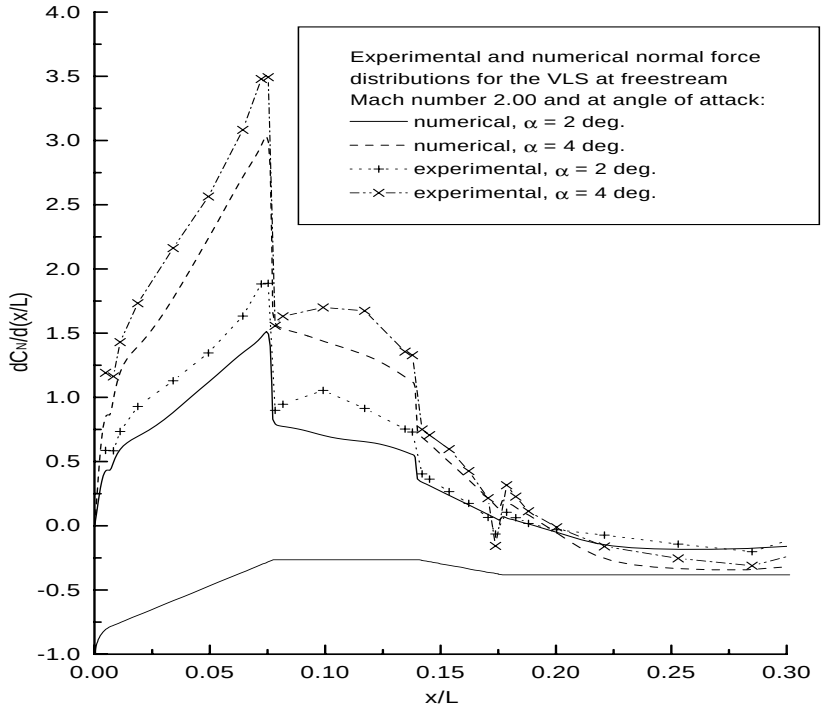

Figure 3: Numerical results for normal force coefficient distribution compared to experimental data for VLS at $\alpha = 2$ and 4 deg. and $M_\infty = 2.00$.

Similar results for the VLS central body at a larger freestream Mach number are presented in Fig. 3. This figures considers flows over the VLS at angles of attack $\alpha = 2$ and 4 deg., and freestream Mach number $M_\infty = 2.00$. One can verify that experimental and numerical curves are qualitatively similar to each other. However, in this case, it is possible to observe that there is a larger difference between computational and experimental data. This difference in the normal force coefficient distribution can be as large as 25% at some longitudinal stations along the VLS central body. At this point in time, the authors believe that the same mechanism that could explain the differences between numerical and experimental data for the $M_\infty = 1.25$ case are responsible for the discrepancies seen in Fig. 3. However, since these differences are considerably larger in this case, additional numerical studies are currently under way in order to try to further assess the correctness of the computations for this $M_\infty = 2.00$ case results.

Results for a higher freestream Mach number, $M_\infty = 3.00$, are presented in Fig. 4 for the case of the VLS central body at angles of attack $\alpha = 2$ and 4 deg. As before, experimental and numerical normal force coefficient distributions are presented in the figure. This case has stronger shock waves present in flow and, hence, it is a more challenging test case for the numerical code. One can observe, however, that the features of the flow are well captured by the code. The same curve patterns seen at Figs. 2 and 3 are observed in this figure as well. As seen in the forebody cone region of Fig. 2, the boundary layer interference in the local flow makes computational distributions less pronounced than the experimental ones. The expansion fan at the end of this region, however, cancels the boundary layer growth and, thus, numerical and wind tunnel results are very close in the payload fairing region.

With the results presented above, the numerical normal force coefficient slope distribution can be obtained from the computational simulations. One should observe that, at angle of attack $\alpha = 0$ deg., the normal force distribution is also zero because the flow is symmetric. Hence, normal force distributions for three different angles of attack are available. Namely, $\alpha = 0$, 2 and 4 deg. Since the VLS is designed to fly at low angles of attack, the best local straight line throughout those three data point is chosen to represent the local slope of the normal force coefficient curve. Results are, then, compared to available experimental data.

Figure 5 presents computational simulation and wind tunnel results for the VLS main body

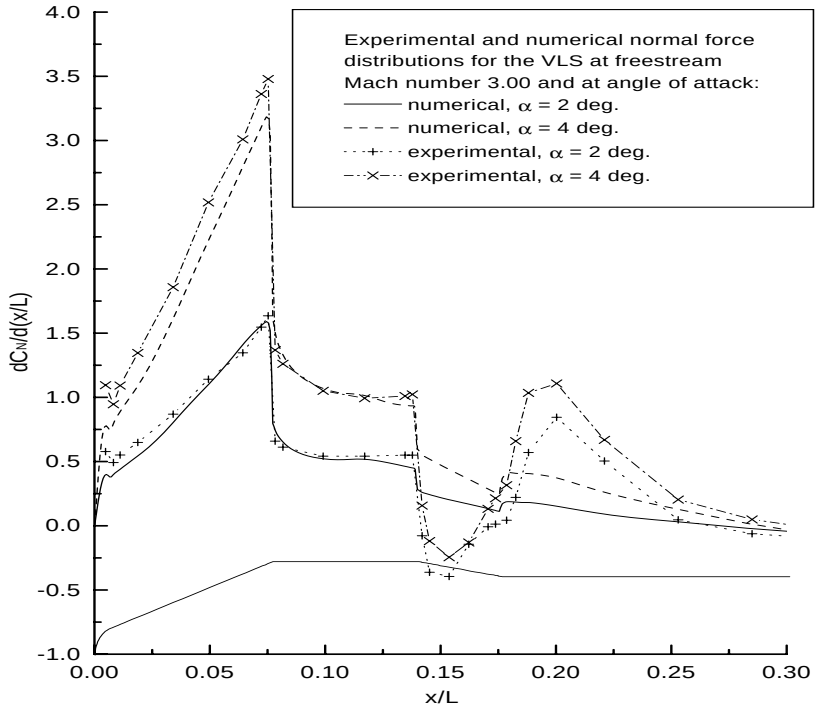

Figure 4: Numerical results for normal force coefficient distribution compared to experimental data for VLS at $\alpha = 2$ and 4 deg. and $M_\infty = 3.00$.

Table 1: Calculated results for the normal force coefficient C_N and the normal force coefficient slope, C_{N_α}, using the numerical and the experimental data.

M_∞	C_N						C_{N_α} (1/deg.)	
	$\alpha = 0$ deg.		$\alpha = 2$ deg.		$\alpha = 4$ deg.			
	Num.	Exp.	Num.	Exp.	Num.	Exp.	Num.	Exp.
1.25	0	0	0.08499	0.09369	0.17164	0.19284	0.04291	0.04667
2.00	0	0	0.10700	0.14241	0.22054	0.26520	0.05514	0.06069
3.00	0	0	0.11849	0.13205	0.24662	0.27934	0.06165	0.07099

at freestream Mach number $M_\infty = 1.25$. The same curve patterns seen in Fig. 2 are observed in this figure as well, as one should expect. Similar results for the VLS central body at a larger freestream Mach number, namely $M_\infty = 2.00$, are presented in Fig. 6. Results for an even higher freestream Mach number, $M_\infty = 3.00$, are presented in Fig. 7 for the VLS central body. As before, the curve patterns of Figs. 6 and 7 are observed in Figs. 3 and 4, respectively. In the three cases presented above, numerical and experimental curves are qualitatively alike. Differences observed, as seen before, can be attributed to the limitations of the inviscid formulation used in the present computations.

The normal force coefficients, C_N, and the normal force slope coefficients, C_{N_α}, are calculated through the integration of the normal force coefficient distributions and the normal force coefficient slope distributions along the body of the rocket. A comparison of these integrated force coefficients is presented in Table 1, where numerical and experimental results for all three angle-of-attack cases are presented. As the previous discussion already indicates, the coefficients obtained through the numerical distribution integrations are smaller than the ones obtained experimentally. One can observe that the differences are usually of the order of 10% for the majority of the cases analyzed. As already discussed, the results for freestream Mach number $M_\infty = 2.00$ have a poorer correlation. Discrepancies for this Mach number are of the order of

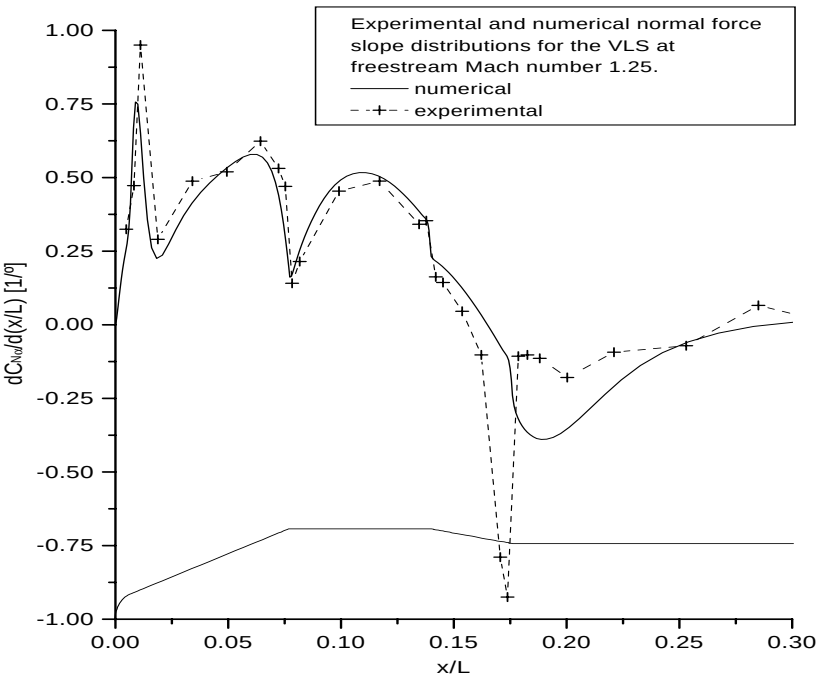

Figure 5: Numerical results for normal force coefficient slope distribution compared to experimental data for VLS at $M_\infty = 1.25$.

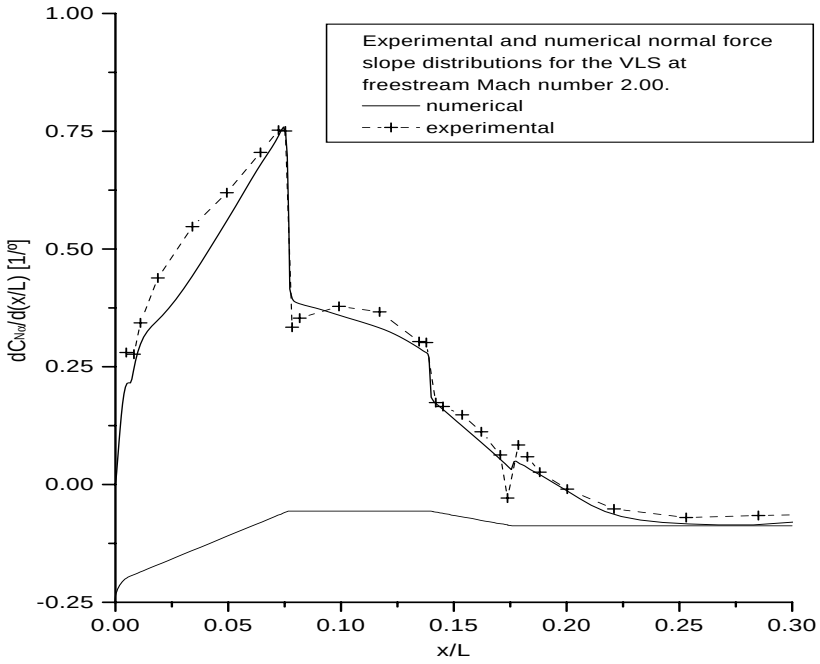

Figure 6: Numerical results for normal force coefficient slope distribution compared to experimental data for VLS at $M_\infty = 2.00$.

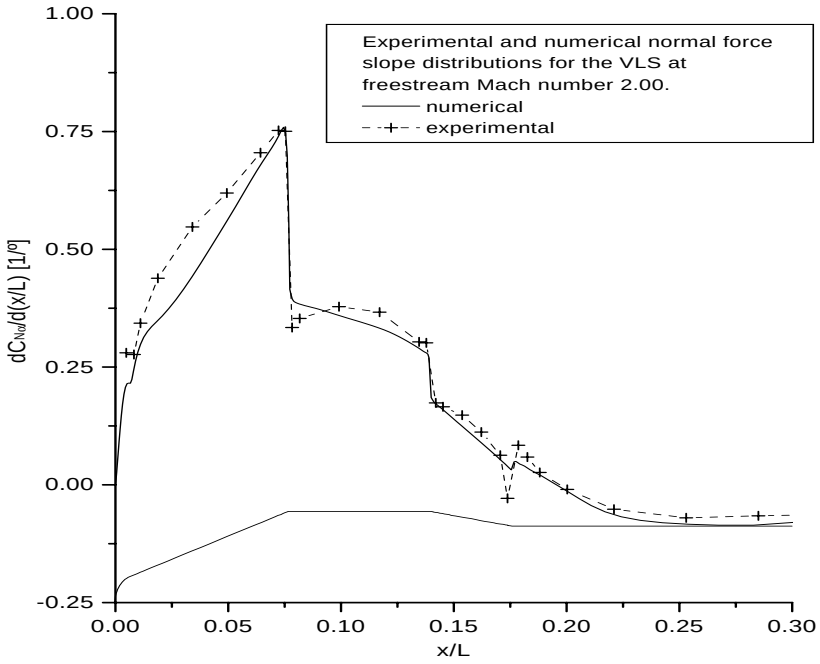

Figure 7: Numerical results for normal force coefficient slope distribution compared to experimental data for VLS at $M_\infty = 3.00$.

25% for the $\alpha = 2$ deg. case and 17% for the $\alpha = 4$ deg. case. It should be observed that errors of about 10% can certainly be considered within the limitations of the inviscid calculations here performed. One could notice that viscous effects are, in general, relevant for launch vehicle configurations due to body bluntness, existence of sharp corners and the overall flight envelope of the vehicle. Therefore, the present Euler calculations should be seen as an evolutionary step towards the desired viscous simulation capability, and an error of 10% indicates that the current calculations could be really used in actual project work.

6. CONCLUDING REMARKS

Numerical simulations for the VLS central body configuration, at freestream Mach numbers 1.25, 2.00 and 3.00 and at angles of attack of 0, 2 and 4 deg., were performed. A solver based on the 3-D compressible Euler formulation, discretized in a finite difference context for general curvilinear coordinates, was used. Time march procedure considered a 5-stage explicit Runge-Kutta scheme and central differences were employed for the spatial discretization. Pressure coefficient distributions along the wall were obtained in order to calculate the normal force coefficient distributions along the vehicle main body. This was performed by an azimuthal integration of the Cp distributions. Normal force coefficient slope distributions were also obtained. Finally, the integrated coefficients were calculated by a longitudinal integration of the various distributions and the computational results were compared to available wind tunnel data.

In general, a very good qualitative agreement between the results was obtained. For most cases, the quantitative agreement was also good, with discrepancies in the integrated coefficients being of the order of 10%. The authors believe that most of the discrepancies can be explained by the limitations of the formulation used in the current simulations, which does not take into account the viscous effects. These can be quite relevant for an accurate description of the flowfield at least over portions of a satellite launcher. On the other hand, the fairly good quantitative agreement of the integrated coefficients is an indication that the present simulations could already be useful for actual vehicle design applications. Moreover, this is also an indication that the numerical code used in this work has the correct capabilities to support further

development, such as the implementation of the full Navier-Stokes equations together with an adequate turbulence model.

Acknowledgments

The present work was partially supported by Conselho Nacional de Desenvolvimento Científico e Tecnológico, CNPq, under the Integrated Project Research Grant No. 522413/96-0. The second author also acknowledges the support from the CNPq/PIBIC program at Instituto Tecnológico de Aeronáutica.

7. REFERENCES

Augusto Neto, A., 1991, VLS/PT-01 – Distribution of normal and lateral force coefficients for the complete vehicle configuration, Report No. 590-0000/B5411, Instituto de Aeronáutica e Espaço, São José dos Campos, SP, Brazil (in Portuguese).

Azevedo, J.L.F., Fico, N.G.C.R.., Jr., and Ortega, M.A., 1995, Two-dimensional and axisymmetric nozzle flow computations using the Euler equations, Journal of the Brazilian Society of Mechanical Sciences, Vol. 17, No. 2, pp. 147-170.

Azevedo, J.L.F., Moraes, P., Jr., Maliska, C.R., Marchi, C.H., and Silva, A.F.C., 1996, Code validation for high-speed flow simulation over satellite launch vehicle, Journal of Spacecraft and Rockets, Vol. 33, No. 1, pp. 15-21.

Azevedo, J.L.F., Zdravistch, F., and Silva, A.F.C., 1991, Implementation and validation of Euler solvers for launch vehicle flows, Proceedings of the Fourth International Symposium on Computational Fluid Dynamics, Vol I, Davis, CA, USA, pp. 42-47.

Bigarelli, E.D.V., and Azevedo, J.L.F., 1999, Calculation of the aerodynamic loads over the Sonda III-A vehicle on transonic and supersonic flow conditions, Report No. 524-000000/-B1001, Instituto de Aeronáutica e Espaço, São José dos Campos, SP, Brazil (in Portuguese).

Bigarelli, E.D.V., Mello, O.A.F., and Azevedo, J.L.F., 1999, Three dimensional flow simulations for typical launch vehicles at angle of attack, 15th Brazilian Congress of Mechanical Engineering, Águas de Lindóia, SP, Brazil.

Jameson, A., and Mavriplis, D., 1986, Finite Volume Solution of the Two-Dimensional Euler Equations on a Regular Triangular Mesh, AIAA Journal, Vol. 24, No. 4, pp. 611-618.

Jameson, A., Schmidt, W., and Turkel, E., 1981, Numerical solution of the Euler equations by finite volume methods using Runge-Kutta time-stepping schemes, AIAA Paper 81-1259, AIAA 14th Fluid and Plasma Dynamics Conference, Palo Alto, CA, USA.

Mello, O.A.F., and Azevedo, J.L.F., 1998, Calculation of the aerodynamic loads over the VLS central body at high angles of attack, Report NT-157/ASE-N/98, Instituto de Aeronaáutica e Espaço, SP (in Portuguese).

Pulliam, T.H., and Steger, J.L., 1980, Implicit finite-difference simulations of three-Dimensional compressible flow, AIAA Journal, Vol. 18, No. 2, pp. 159-167.

Turkel, E., and Vatsa, V.N., 1994, Effect of artificial viscosity on three-dimensional flow solutions, AIAA Journal, Vol. 32, No. 1, pp. 39-45.

Ying, S.X., 1986, Three-dimensional implicit approximately factored schemes for the equations of gasdynamics, SUDAAR 557, Dept. of Aeronautics and Astronautics, Stanford University, Stanford, CA, USA.

Zdravistch, F., and Azevedo, J.L.F., 1990, Numerical simulation of high speed flows over complex satellite launchers, 3rd Brazilian Congress of Engineering and Thermal Sciences – ENCIT-90, Itapema, SC, Brazil.